

1 **Lower urban humidity moderates heat stress**

2 T. Chakraborty^{1,3,*}, Z. S. Venter², Y. Qian³, X. Lee^{1,*}

3

4 ¹School of the Environment, Yale University, New Haven, CT, USA

5 ²Terrestrial Ecology Section, Norwegian Institute for Nature Research—NINA, 0349 Oslo,
6 Norway

7 ³Pacific Northwest National Laboratory, Richland, WA, USA

8

9

10

11 **Key Points**

- 12 • Lower humidity and higher air temperature in cities compared to rural backgrounds
13 compensate for each other to moderate heat stress
- 14 • Radiative skin temperature is a poor proxy for both intra-urban heterogeneity and
15 variability in urban-rural difference in heat stress
- 16 • Vegetation is much less efficient at reducing heat stress than at reducing satellite-derived
17 skin temperature

18

19 **Key words:** Heat stress; urban climate; humidity; crowdsourced data; remote sensing; urban
20 vegetation

21

22 *Corresponding authors: T. Chakraborty (tc.chakraborty@pnnl.gov) and X. Lee
23 (xuhui.lee@yale.edu)

24 **Abstract**

25 Radiative skin temperature is often used to examine heat exposure in multi-city studies and for
26 informing urban heat management efforts since urban air temperature is rarely measured at the
27 appropriate scales. Cities also have lower relative humidity, which is not traditionally accounted
28 for in large-scale observational urban heat risk assessments. Here using crowdsourced
29 measurements from over 40,000 weather stations in ≈ 600 urban clusters in Europe, we show the
30 moderating effect of this urbanization-induced humidity reduction on heat stress during the 2019
31 heatwave. We demonstrate that daytime differences in heat index between urban clusters and
32 their surroundings are weak and associations of this urban-rural difference with background
33 climate, generally examined from the skin temperature perspective, is diminished due to
34 moisture feedback. We also examine the spatial variability of skin temperature, air temperature,
35 and heat indices within these clusters, relevant for detecting hotspots and potential disparities in
36 heat exposure, and find that skin temperature is a poor proxy for the intra-urban distribution of
37 heat stress. Finally, urban vegetation shows much weaker ($\sim 1/6^{\text{th}}$ as strong) associations with
38 heat stress than with skin temperature, which has broad implications for optimizing urban heat
39 mitigation strategies. Our results are valid for both operational metrics of heat stress (such as
40 apparent temperature and Humidex) and for various empirical heat indices from epidemiological
41 studies. This study provide large-scale empirical evidence that skin temperature, used due to the
42 lack of better alternatives, is weakly suitable for informing heat mitigation strategies within and
43 across cities, necessitating more urban meteorological observations.

44

45 **Plain Language Summary**

46 A central theme in urban climatology is that cities have higher heat stress than their background
47 rural landscapes. In scientific studies across many cities, satellite observations are often used as a
48 proxy for this higher urban heat stress. However, satellites measure the temperature of the urban
49 surface, while heat stress is mainly a function of air temperature and humidity. It is critical to
50 know how well, if at all, satellites capture urban heat stress, which has been traditionally difficult
51 to measure using ground observations due to the lack of weather stations in cities. Here, we use
52 measurements from over 40,000 citizen weather stations over Europe to address this important
53 gap and compare the distributions of satellite-derived surface temperature, air temperature, and
54 heat stress during the July 2019 heatwave. We find that the lower relative humidity due to
55 urbanization partly offsets the effect of higher air temperatures on urban heat stress. Moreover,
56 satellite-derived surface temperature shows very weak relationships with air temperature and
57 heat stress, both within cities and when examining urban-rural differences across cities. Finally,
58 urban vegetation is much less effective at reducing heat stress than at reducing surface
59 temperature. These results are relevant for informing future urban research.

60 1. Introduction

61 As the world continues to warm, with heatwaves becoming more frequent and intense (Perkins-
62 Kirkpatrick & Lewis, 2020), urban areas are expected to face the brunt of the impacts due to
63 large populations and higher temperatures (Heaviside et al., 2017; Heilig, 2014). That cities, on
64 average, have higher temperatures than their surroundings – the urban heat island (UHI) effect –
65 is well-established (Arnfield, 2003; Qian et al., 2022). However, the time and magnitude of this
66 phenomenon varies substantially across cities and depends on the type of temperature
67 measurement (Ho et al., 2016; Venter et al., 2021; Zhang et al., 2014). Even though UHI
68 estimates were traditionally from air temperature (T_a) measurements (Howard, 1833), many
69 recent large-scale observational and modeling studies on the UHI, and urban climate in general,
70 have focused on radiative skin temperature (T_s) (Chakraborty et al., 2019; Chakraborty & Lee,
71 2019; Clinton & Gong, 2013; Hoffman et al., 2020; Hsu et al., 2021; Manoli et al., 2019;
72 Mentaschi et al., 2022; Schwaab et al., 2021; L. Zhao et al., 2014, 2017), with many of these
73 studies commenting on heat exposure in cities, their public health consequences, and potential
74 mitigation strategies. Similarly, maps derived from T_s are often used as a guide for planning heat
75 mitigation strategies by decision makers (Keith et al., 2019). However, T_a is more relevant for
76 heat exposure than T_s , but is difficult to measure in cities due to the dearth of standard weather
77 stations and hard to model due to multiple confounding factors (Ho et al., 2016; Muller et al.,
78 2013; Stone Jr et al., 2019). The two variables – T_a and T_s – are physically distinct (Jin &
79 Dickinson, 2010), and the urban-rural differences in T_a (ΔT_a) and T_s (ΔT_s) are also not well
80 correlated (Venter et al., 2021; Zhang et al., 2014), which brings into question the potential
81 public health and policy implications of urban studies using T_s .

82 Urban areas may also be drier than their surroundings (particularly in humid climate) due to the
83 removal of vegetation and pervious surfaces - the urban dry island (UDI) effect (Lokoshchenko,
84 2017; Qian et al., 2022). In comparison to the multitude of studies on the UHI, the UDI is rarely
85 considered in large-scale urban heat risk assessments due to the lack of consensus on a standard
86 metric for urban moisture content (Z. Wang et al., 2021) and the difficulty in measuring near-
87 surface moisture within cities, even when using satellites. The human physiological response to
88 heat depends not just on T_a , but also on relative humidity (RH) (Anderson et al., 2013; Raymond
89 et al., 2020; Sherwood & Huber, 2010). Electricity demand for cooling buildings, expected to be

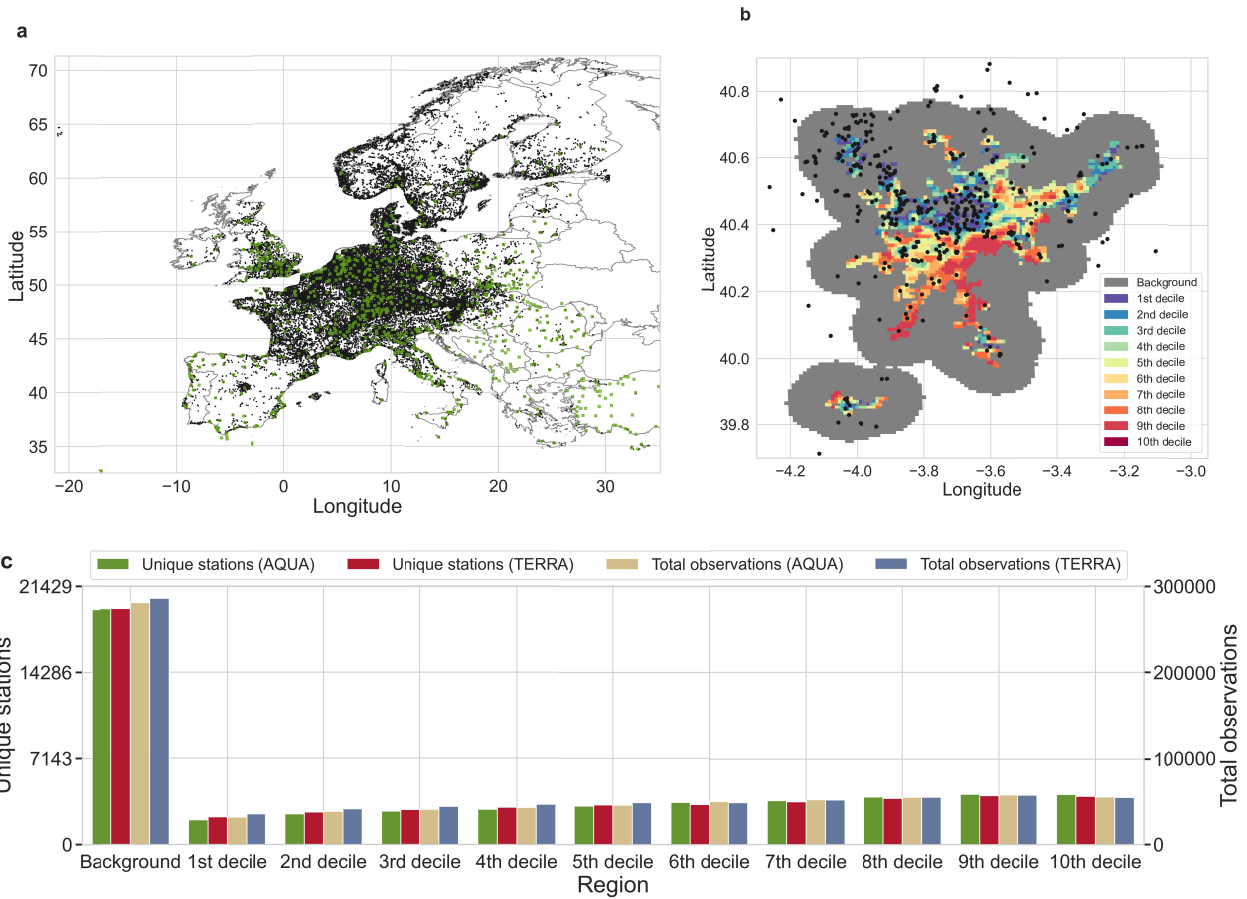
90 enhanced due to the UHI, also depends on atmospheric humidity (Maia-Silva et al., 2020).
91 Therefore, a more accurate understanding of the impact of urbanization on public health, energy
92 demand, and the economy should account for the combined impacts of T_a and RH. Although
93 modeling studies have the freedom to examine simulated T_a and RH (and thus, heat stress) over
94 urban areas (Huang et al., 2021; Oleson et al., 2015; Sarangi et al., 2021; L. Zhao et al., 2021),
95 models use simplified representations of urban areas with multiple sources of uncertainty
96 (Krayenhoff et al., 2021; Qian et al., 2022; Sharma et al., 2021; Zheng et al., 2021).
97 Additionally, it is computationally expensive to run such models at fine-enough scales to resolve
98 intra-urban variability.

99 Here we combine dense citizen weather station (CWS) measurements and satellite observations
100 over Europe during the July 2019 heatwave to comprehensively examine the distributions of T_s ,
101 T_a , RH, and heat stress within and across satellite-derived urban clusters. We consider several
102 metrics, both empirical and thermodynamic, for estimating heat stress, including the apparent
103 temperature used by the US National Weather Service (HI_0), which describes what the
104 temperature feels like to humans when humidity is accounted for (Rothfusz, 1990; Steadman,
105 1979). Our results, based on measurements from over 40,000 (after quality control) CWSs in
106 over 600 clusters, suggest that the lower RH in these cities partially cancels out the impact of
107 higher T_a on heat stress during daytime, resulting in smaller differences in HI_0 (and several other
108 heat indices considered) between urban areas and their surroundings. We also analyze the spatial
109 gradients of these variables within clusters and demonstrate that satellite-derived T_s poorly
110 captures the spatial distribution of ambient HI_0 within cities. Finally, with reference to the notion
111 of employing urban vegetation to reduce local-scale heat stress, we find that vegetation is much
112 less efficient at lowering HI_0 than lowering T_s at these scales. These results demonstrate the
113 contrasting roles T_a and RH play to moderate urbanization-induced heat stress across scales - the
114 most comprehensive analysis of this sort using *in situ* observations - and suggest that we should
115 re-evaluate the current dependence on satellite-derived insights for urban design and policy
116 making.

117 **2. Methods**

118 **2. 1 Urban clusters and their rural backgrounds**

119 Urban clusters over Europe are the primary regions of interest for our analysis. These clusters
 120 were generated by vectorizing contiguous 1 km x 1 km pixels classified as either low- or high-
 121 density urban in the Global Human Settlement Layer’s (GHSL) settlement classification dataset
 122 (version R2016A) (Pesaresi & Freire, 2016). This aggregation of the connected urban pixels into
 123 individual urban cluster polygons is done on the Google Earth Engine cloud computing platform
 124 (Gorelick et al., 2017). Since many of these clusters are small and do not have enough citizen
 125 weather station (CWS) observations, clusters smaller than the 50th percentile of the urban cluster
 126 area distribution are removed, leaving 929 clusters (Fig. 1a).



129 **Fig. 1** Regions of interest and data summary. Sub-fig **a** shows the spatial distribution of Netatmo
 130 stations (black dots) over Europe during the heatwave of July 2019, as well as the urban clusters
 131 (in green) in the region. Sub-fig **b** shows an example of the daytime ($\approx 1:30$ pm) surface
 132 temperature (T_s) decile neighborhoods within an urban cluster (from up to 10th to 90th-100th
 133 percentile) based on daily MODIS Aqua scenes. Similar regions are created corresponding to

134 Terra observations (not shown). The black dots show the Netatmo stations over the cluster and
135 the gray region represents the rural reference. Sub-fig **c** shows the total number of valid
136 observations and unique stations for each region that correspond to the Terra and Aqua overpass
137 times.

138 The rural or background reference for each cluster is a polygon buffer of 10 km width
139 surrounding it (Fig. 1b), a definition of rural reference used in a previous global-scale study
140 (Clinton & Gong, 2013). Since some urban clusters are closer to each other than 20 kms, a focal
141 mode smoothing function is applied to prevent any overlap between the rural references of
142 nearby clusters. This function designates a border between two overlapping buffers such that
143 they are equidistant to the original urban clusters they surround. More information about the
144 generation of the urban clusters and their rural references can be found in Venter et al. (Venter et
145 al., 2021).

146 **2.2 Citizen weather station data**

147 All hourly T_a and RH observations from CWSs over Europe were downloaded for July 2019
148 from Netatmo (<https://netatmo.com/>). This includes data from 113,215 stations during this
149 period. CWSs data have errors and biases related to less-than-ideal sensor placement, insufficient
150 site metadata, lack of radiation shield, and instrumental errors (Meier et al., 2017). We follow a
151 quality-control procedure developed for these sensors using the “Crowd-QC” package in R
152 (Napoly et al., 2018). The quality-control procedure starts with removal of statistical outliers
153 using a modified z-score approach and the hourly T_a distributions. Then, sites for which the
154 measured T_a , when correlated against the spatial median of monthly T_a , show Pearson’s
155 correlation coefficients less than 0.9, are removed. These steps reduce the number of available
156 stations to 95,084.

157 Since we wanted to get representative values for July 2019, we also removed Netatmo stations
158 with more than 20% missing data during this period, leaving 75,293 stations. This threshold was
159 found sufficient to capture the monthly climatological state in a previous study (Venter et al.,
160 2021). We note that most of the quality-control procedure has been developed for T_a , not RH.
161 However, since the Netatmo sensor module houses both T_a and RH sensors, issues related to
162 sensor misplacement and instrumental errors would also minimize errors in measured RH. This

163 is also confirmed through validation of the CWS measurements (see corresponding subsection
164 below).

165 **2.3 Calculating apparent temperature and other heat indices**

166 Since humans primarily thermoregulate through sweating, the moisture content of the air limits
167 our body's ability to dissipate heat, making it an important factor in addition to T_a when studying
168 heat stress (Sherwood & Huber, 2010). There are multiple metrics of heat stress that account for
169 moisture. In the present study, we use the heat index used by the US National Weather Service
170 (NWS), also known as apparent temperature. This index (HI_0) is calculated in multiple steps. We
171 start with a simple formula whose results are consistent with those from Steadman, 1979
172 (Steadman, 1979):

$$173 \quad HI_0 = 0.5 \times [T_a + 61 + [(T-68) \times 1.2] + (0.094RH)] \quad (1)$$

174 where T_a is in °F and RH is in percentage. If the average of T_a and this heat index is less than 80
175 °F, this is the final equation used. If the average is equal to or above 80°F, the Rothfus
176 regression (Rothfusz, 1990) is used instead, given by:

$$\begin{aligned} HI_0 = & -42.379 + 2.04901523T_a + 10.14333127RH - 0.22475541T_aRH - 6.83783 \\ & \times 10^{-3}T_a^2 - 5.481717 \times 10^{-2}RH^2 + 1.22874 \times 10^{-3}T_a^2RH + 8.5282 \\ & \times 10^{-4}T_aRH^2 - 1.99 \times 10^{-6}T_a^2RH^2 \end{aligned} \quad (2)$$

177 Similar to Eq. 1, the T_a is input in °F. Additional adjustments are made for low and high values
178 of RH, consistent with the method used in operational heat warning systems by the US NWS
179 (Rothfusz, 1990).

180 To check the consistency of our results, we also consider several other empirical approximations
181 of heat stress that combine the impact of T_a and moisture, including the humidex (Masterton &
182 Richardson, 1979) and one of each functional forms of the heat index approximation in °C
183 reviewed in Anderson et al. (2013)

184 The humidex can be expressed as:

$$185 \quad \text{Humidex} = T_a + 0.5555 \times \left(6.11 \times e^{5417.753 \times \left(\frac{1}{273.16} - \frac{1}{273.15 + T_D} \right)} - 10 \right) \quad (3)$$

186 where T_D is the dew-point temperature in °C and is given by:

$$187 \quad T_D = \frac{243.04 \times \left\{ \ln\left(\frac{RH}{100}\right) + \frac{17.625 \times T_a}{243.04 + T_a} \right\}}{17.625 - \left\{ \ln\left(\frac{RH}{100}\right) + \frac{17.625 \times T_a}{243.04 + T_a} \right\}} \quad (4)$$

188 Finally, the other four functional forms of the heat index considered here are denoted by HI_1 ,
189 HI_2 , HI_3 , and HI_4 and given by:

$$190 \quad HI_1 = T_a - 1.0799e^{0.03755T_a} (1 - e^{0.0801(T_D - 14)}) \quad (5)$$

$$191 \quad HI_2 = -2.653 + 0.994T_a + 0.0153T_D^2 \quad (6)$$

$$192 \quad HI_3 = -8.7847 + 1.6114T_a - 0.012308T_a^2 \\ + RH[2.3385 - 0.14612T_a + (2.2117 \times 10^{-3})T_a^2] \\ + RH^2[-0.016425 + (7.2546 \times 10^{-4})T_a + (-3.582 \times 10^{-6})T_a^2] \quad (7)$$

$$193 \quad HI_4 = T_a - 0.55 \times (1 - 0.001RH)(T_a - 14.5) \quad (8)$$

194 In addition to these heat indices, we also calculate the wet-bulb temperature (T_w), a
195 thermodynamic measure of how effectively humans can cool down via sweating (Sherwood &
196 Huber, 2010) and a metric for heat stress often used in climate-related studies (Mishra et al.,
197 2020; Raymond et al., 2020; L. Zhao et al., 2021), using the formulation proposed by Stull
198 (2011).

199 **2.4 Research-grade weather station data**

200 To evaluate the CWS measurements, we acquired observations from the European Climate
201 Assessment & Dataset (ECA&D) weather stations (ECA&D, 2013) for July 2019. The ECA&D
202 dataset provides daily observations from meteorological stations throughout Europe. We extract
203 daily T_a and RH from this network and calculate HI_0 using Eqs 1 and 2.

204 **2.5 Reanalysis data**

205 We also extract hourly and monthly T_a , T_D (RH is not provided by this dataset), surface pressure,
206 and accumulated precipitation from the ECMWF (European Centre for Medium-Range Weather
207 Forecasts) Reanalysis 5th Generation Land (ERA5-Land) dataset (Muñoz-Sabater et al., 2021).
208 The ERA5-Land provides surface variables at high (≈ 9 km) resolution and is based on the tiled
209 ECMWF Scheme for Surface Exchanges over Land incorporating land surface hydrology (H-
210 TESSEL) and is constrained by multiple observational datasets (Muñoz-Sabater et al., 2021).

211 The hourly RH is computed by dividing the saturation vapor pressure (e_s) at T_D by the saturation
212 vapor pressure at T_a , both calculated using the Clausius-Clapeyron equation (Iribarne & Godson,
213 1981). Thus:

$$214 \text{ RH} = 100 \times \frac{e_s(T_D)}{e_s(T_a)} \quad (9)$$

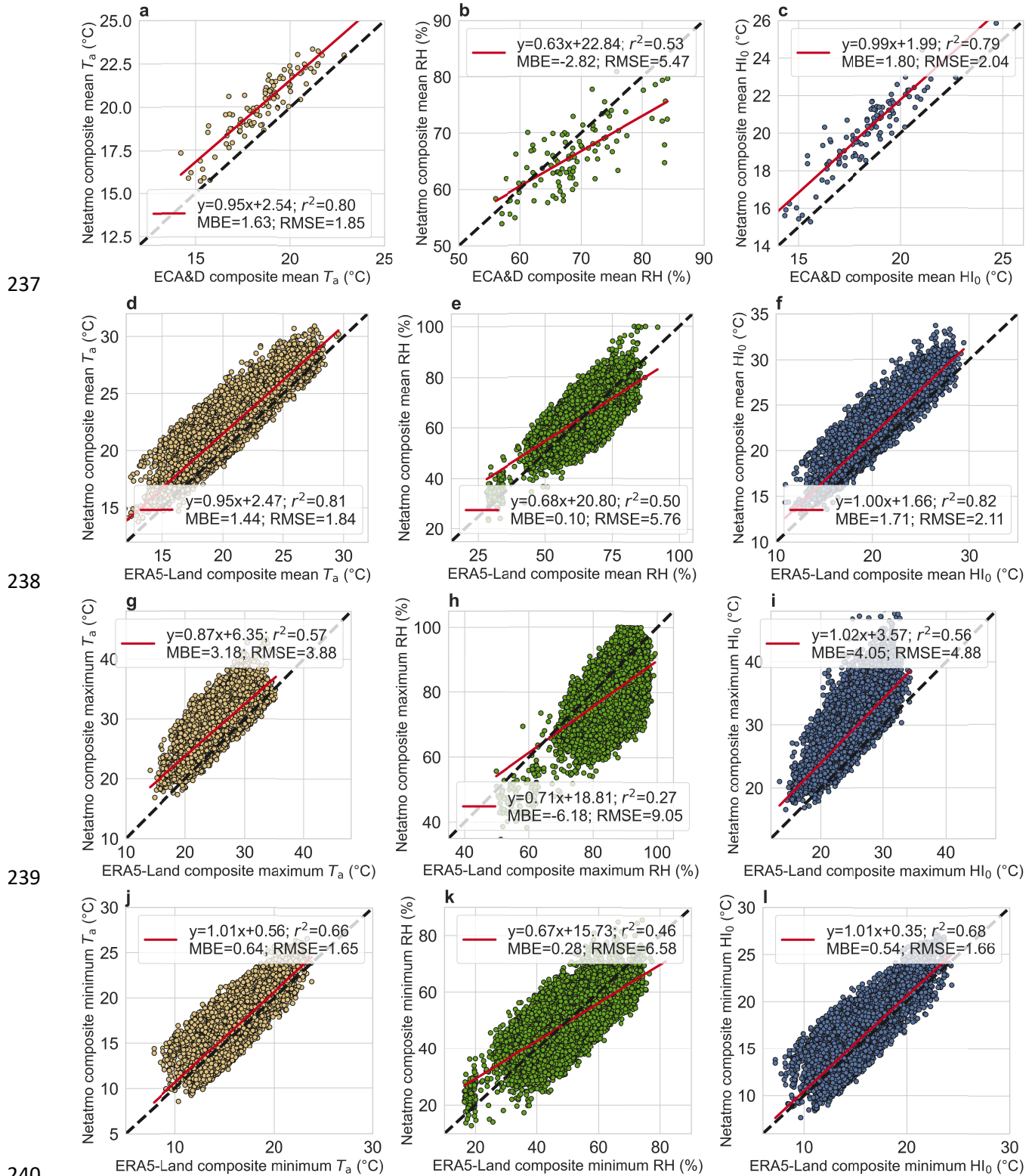
$$215 e_s(T) = 6.11e^{\left[\frac{L_v}{R_v} \left(\frac{1}{273.15} - \frac{1}{T}\right)\right]} \quad (10)$$

216 where T is the temperature (either T_a or T_D) in Kelvin, L_v is the latent heat of vaporization of
217 water ($2.501 \times 10^6 \text{ J kg}^{-1}$), and R_v is the specific gas constant for water vapor ($461 \text{ J K}^{-1} \text{ kg}^{-1}$).

218 **2.6 Validating citizen weather station data**

219 Since the ECA&D weather stations are generally not set up in cities, we start by matching each
220 ECA&D station with rural Netatmo stations that are within a buffer of 2000 m. Some of the
221 ECA&D stations have daily mean RH of 100% for almost the entire month, which is physically
222 implausible. These are removed from the analysis. For each day that measured T_a and RH are
223 available for a valid ECA&D station, we choose the corresponding Netatmo stations that include
224 all 24 hours of observations to reliably compute the daily means. The composite means for the
225 whole period (July 2019) from ECA&D and the Netatmo sensors are then correlated (Figs. 2a to
226 2c). A few of the Netatmo sensors show implausibly large differences in mean daily T_a ($>10 \text{ }^\circ\text{C}$)
227 from the corresponding ECA&D measurements. To account for this in a statistically robust
228 manner, we remove Netatmo stations whose difference in measured T_a and RH with its nearby
229 ECA&D station is above 99 percentile or below 1 percentile of the whole distribution. These
230 stations are not used for any of the subsequent analyses.

231 Overall, the CWS-measured T_a and RH show strong correlations with ECA&D observations (r^2
232 = 0.8 and 0.53, respectively; Figs. 2a and 2b) during this period. The root-mean-square-error
233 (RMSE) and mean bias error (MBE) are both reasonably small (RMSE = 1.85 $^\circ\text{C}$ and MBE =
234 1.63 $^\circ\text{C}$ for T_a ; 5.47% and -2.82% for RH). The Netatmo sensors overestimate T_a and
235 underestimate RH, which would be expected if they often lack radiation shields (Da Cunha,
236 2015). However, the distribution of HI_0 is well captured by these sensors (Fig. 2c).



241 **Fig. 2** Validation of citizen weather station data. Composite mean Netatmo **a** air temperature
 242 (T_a), **b** relative humidity (RH), and **c** heat index (HI_0) against corresponding European Climate

243 Assessment & Dataset (ECA&D) weather stations for the whole study period (July 2019). Sub-
244 figures **d, e, f, g, h, i, j, k, and l** show composite mean (**d, e, and f**), maximum (**g, h, and i**), and
245 minimum (**j, k, and l**) Netatmo observations against corresponding ECMWF (European Centre
246 for Medium-Range Weather Forecasts) Reanalysis 5th Generation Land (ERA5-Land) gridded
247 values. Each dot represents a composite value and the corresponding metrics for evaluation are
248 shown in the legend.

249 The use of daily mean values for evaluation would underestimate the biases caused due to the
250 lack of radiation shields during daytime. Although the ECA&D dataset includes maximum and
251 minimum T_a for each station, it only includes daily mean RH, which would not allow us to
252 calculate the maximum and minimum HI_0 . Instead, we use the maximum and minimum
253 composite values (in addition to daily means) from ERA5-Land data to compare against the
254 corresponding rural Netatmo measurements (Figs. 2d to 2l) after removing daily differences
255 greater than 99 percentile and less than 1 percentile of the distribution. Consistent with the
256 comparisons with ECA&D, the Netatmo measurements overestimate T_a and HI_0 (Fig. 2d, 2f).
257 The maximum composite T_a , which would be generally in the early afternoon (Fig. S1a), is
258 overestimated more (MBE = 3.18 °C) than the mean composite T_a (MBE = 1.44 °C). For
259 minimum values, generally during early morning, the biases are much smaller, with even smaller
260 biases for HI_0 (Fig. 2l). For all cases, there is compensation between the biases due to T_a and RH,
261 leading to slopes closer to 1 for HI_0 than for T_a .

262 Note that the larger spread between the ERA5-Land and Netatmo is expected since these
263 estimates are at different scales. A Netatmo measurement represents information for a small
264 footprint around the CWS, while the ERA5-Land estimate is for a ≈ 9 km grid overlaying that
265 Netatmo site. Although there are biases between the Netatmo data and the point and gridded
266 estimates, the distributions are captured well by the CWSs, particularly for T_a and HI_0 , with
267 slopes close to 1 (Fig. 2). Since we focus on the spatial distribution of these variables (within and
268 between cities), not their absolute magnitudes, we are confident about our results.

269 **2.7 Decile neighborhoods of urban skin temperature**

270 To estimate the gradient of mean T_s within urban clusters during the study period, we first
271 calculate the 10th to 100th percentile of T_s within each cluster using Moderate Resolution Imaging

272 Spectroradiometer (MODIS) observations (MYD11A1.006 and MOD11A1.006) (Wan, 2006).
273 These percentile values are from the mean pixel-level information (by averaging available daily
274 satellite scenes) for July 2019. Different percentile values are obtained for the four cases, namely
275 Terra daytime overpass ($\approx 10:30$ am local time), Aqua daytime overpass ($\approx 1:30$ pm local time),
276 Terra nighttime overpass ($\approx 10:30$ pm local time), and Aqua nighttime overpass ($\approx 1:30$ am local
277 time). Of these, we focus mostly on the daytime values, particularly for the Aqua overpass,
278 which is close to the time of maximum T_a and HI_0 (Fig. S1). Using these percentile values as
279 boundary conditions, we separate each urban cluster into 10 decile neighborhoods, with each
280 neighborhood representing a decile of T_s variation. In other words, pixels with July mean T_s
281 values between $>0^{\text{th}}$ and 10^{th} percentile of all mean T_s values in a cluster are put into the 10^{th}
282 percentile neighborhood (or first decile neighborhood), and so on till the 100^{th} percentile
283 neighborhood or 10^{th} decile neighborhood, which includes mean T_s values between $>90^{\text{th}}$ and
284 100^{th} percentile. The decile neighborhoods are different for Terra and Aqua as well as for days
285 and nights. An example of these decile neighborhoods is shown for Madrid, Spain in Fig. 1b.
286 Note that, for this particular cluster, the T_s gradient does not increase as we reach the city center.
287 This is intended since our goal is to examine whether the decile neighborhoods, as determined by
288 satellite observations (as has been frequently done in recent studies), is a reasonable proxy for
289 the T_a and heat stress gradients.

290 After the decile neighborhoods are generated, each Netatmo station is grouped into a
291 neighborhood for the four cases corresponding to the satellite overpass times. All these
292 geospatial analyses are done on the Google Earth Engine platform (Gorelick et al., 2017).

293 **2.8 Matching CWS data with satellite-derived estimates**

294 We extract the daily T_s and exact MODIS viewing time for each ≈ 1 km pixel corresponding to
295 the Netatmo stations that are either in a T_s decile neighborhood or in the rural background. The
296 satellite viewing time is then converted from local time to coordinated universal time (UTC)
297 based on the recommendations in the MODIS user guide (Wan, 2006) of subtracting (in hours)
298 the quotient when dividing the longitude of the pixel (in this case, the CWS location) by 15
299 degrees and then adjusting by the daily hour bounds (>24 hours or <0 hours). The Netatmo
300 observations are then matched with the daily MODIS T_s when the Netatmo observation time is
301 within 30 minutes of the MODIS viewing time.

302 Similar to T_s , we also extract the Normalized Difference Vegetation Index (NDVI), a satellite-
 303 derived proxy for live green vegetation (Rouse et al., 1974), from MODIS observations. This
 304 index takes advantage of the fact that plants absorb light in the red (RED) bands and reflect near-
 305 infrared (NIR) radiation since it cannot be used photosynthesis, and is given by:

$$306 \quad \text{NDVI} = \frac{\text{NIR}-\text{RED}}{\text{NIR}+\text{RED}} \quad (11)$$

307 The NDVI values are derived from 16-day composites corresponding to each Netatmo station
 308 and daytime overpass (MYD13A2 and MOD13A2 for Aqua and Terra, respectively) and joined
 309 with all observations at that station. The monthly means of NDVI for July 2019 are used for the
 310 final analysis since daily variability is not as relevant for NDVI and urban surface vegetation
 311 would remain relatively unchanged within a single month. In all cases, only clear-sky pixel
 312 values are used for analysis and satellite observations for the days with missing Netatmo
 313 observations (both T_a and RH) due to quality-screening are also removed.

314 We also calculate monthly precipitation rate corresponding to each cluster from the monthly
 315 composite generated from the passive-microwave observations from the Global Precipitation
 316 Measurement (GPM) mission (NASA Goddard Earth Sciences Data And Information Services
 317 Center, 2019). This is done to examine how urban-rural differences in the variables of interest
 318 (see below) vary with the moisture availability of the background climate.

319 **2.9 Urban-rural differences**

320 Netatmo stations within the urban clusters and their corresponding satellite-derived values are
 321 used to estimate the urban T_a ($T_{a,u}$), RH (RH_u), HI_0 ($\text{HI}_{0,u}$), T_s ($T_{s,u}$), and NDVI (NDVI_u). The
 322 corresponding rural variables, $T_{a,r}$, RH_r , $\text{HI}_{0,r}$, $T_{s,r}$, and NDVI_r are from the stations in the
 323 background reference areas. Only those cases were considered for which there were at least 10
 324 stations in both the urban clusters and their surrounding references. This leaves 557 (603) urban
 325 clusters with 40560 (42745) unique stations for Aqua (Terra) daytime overpass. The urban-rural
 326 differences are thus:

$$327 \quad \Delta T_a = T_{a,u} - T_{a,r} \quad (12)$$

$$328 \quad \Delta \text{RH} = \text{RH}_u - \text{RH}_r \quad (13)$$

$$329 \quad \Delta \text{HI}_0 = \text{HI}_{0,u} - \text{HI}_{0,r} \quad (14)$$

330 $\Delta T_s = T_{s,u} - T_{s,r}$ (15)

331 $\Delta \text{NDVI} = \text{NDVI}_u - \text{NDVI}_r$ (16)

332 Of these, ΔT_a is equivalent to the commonly studied canopy urban heat island (CUHI) and ΔT_s is
 333 the surface urban heat island (SUHI) (Bonafoni et al., 2015; Chakraborty et al., 2017; Du et al.,
 334 2021; Venter et al., 2021). Although RH is a function of both absolute moisture content and
 335 ambient temperature, we call its urban-rural differences the urban dry island (UDI) effect since it
 336 is one of the variables used to estimate HI_0 (Eq. 1). There is currently lack of consensus on a
 337 standard metric for urban moisture content, though it is commonly accepted that urban areas are
 338 drier due to removal of vegetation and pervious surfaces (Z. Wang et al., 2021). For comparison,
 339 we also calculate the difference in absolute humidity (AH) between urban areas and their
 340 background references by combining the Netatmo observations with surface pressure estimates
 341 from ERA5-Land (Muñoz-Sabater et al., 2021). During the Aqua daytime overpass, roughly
 342 54.3% of the urban clusters show lower AH than their background references with a mean ΔAH
 343 of $-8.7 \times 10^{-5} \text{ kg m}^{-3}$, confirming the presence of UDIs using both RH and AH. Similar urban-rural
 344 differences are also calculated for the Humidex and the other heat indices. The use of the
 345 MODIS pixels overlaying the Netatmo locations to calculate ΔT_s leads to reasonable apples-to-
 346 apples comparison. This might explain why our correlation coefficient between ΔT_s and ΔT_a
 347 (Fig. 7a) is slightly higher than that in a previous study (Venter et al., 2021), which compared the
 348 Netatmo-derived ΔT_a with urban cluster mean ΔT_s .

349 **2.10 Intra-urban gradients**

350 Although the analysis above is done for co-located pixels, the threshold for the minimum number
 351 of stations used (10) is insufficient to represent the mean climatic state of the clusters. Moreover,
 352 it is important to also analyze how well T_s , which has been extensively used as a proxy for the
 353 intra-urban variability in urban temperatures (Benz & Burney, 2021; Chakraborty et al., 2019,
 354 2020; Hoffman et al., 2020; Hsu et al., 2021; Hulley et al., 2019), represents the within-city
 355 variability in HI_0 . To address this, we estimate the intra-urban gradients in T_s , T_a , RH, and HI_0 .
 356 The intra-urban gradient in station-level T_s is calculated by first choosing those clusters with at
 357 least 10 stations in every decile neighborhood as well as the rural background, and then
 358 averaging the daily pixel-level MODIS T_s in July 2019 that also had CWS measurements of T_a
 359 and RH for each region. This analysis allows us to check how well the Netatmo observations

360 capture the overall spatial variability in T_s , as represented by the decile neighborhoods, using the
 361 corresponding T_s pixels overlaying those stations. The average value of the satellite-derived T_s
 362 for the pixels overlaying the Netatmo stations increase for increasing decile neighborhoods in all
 363 clusters (Figs. 2, S4). Similarly, the gradients corresponding to these regions for T_a , RH, and thus
 364 HI_0 are computed from the corresponding hourly Netatmo measurements. Figure 1c shows the
 365 total number of observations as well as the number of unique Netatmo stations considered when
 366 calculating these intra-urban gradients corresponding to the Terra and Aqua daytime overpass.
 367 Overall, we use 153 and 155 clusters to generate intra-urban gradients corresponding to Aqua
 368 and Terra daytime overpass.

369 2.11 Statistical analysis

370 To check whether the distributions of the chosen variables (T_s , T_a , RH, HI_0 , Humidex, HI_1 , HI_2 ,
 371 HI_3 , and HI_4) are statistically different between regions (either between urban clusters and their
 372 rural backgrounds or between the rural backgrounds and the decile neighborhoods), we use the
 373 Mann –Whitney two-sample test (Wilcoxon et al., 1992). This nonparametric test allows us to
 374 check if two samples come from the same population, with lower p-values supporting the
 375 rejection of the null hypothesis that both the distributions are same. We choose a significant level
 376 of 0.01 to reject the null hypothesis, but also specify when the p-value is below 0.001 and 0.0001
 377 in the summary tables (Tables S1, S2, S3, S4).

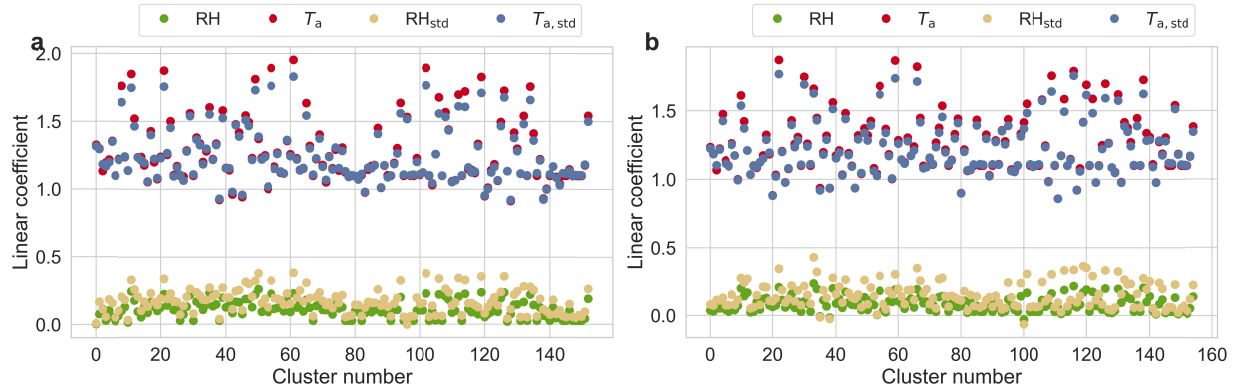
378 In addition to simple linear regressions between pairs of variables to test for their correlation and
 379 sensitivity, we also separate the control of T_a and RH on the intra-urban gradient of HI_0 within
 380 clusters by representing HI_0 as a linear combination of T_a and RH:

$$381 \quad HI_0 = \alpha_1 T_a + \alpha_2 RH \quad (17)$$

382 where α_1 and α_2 are the sensitivities of HI_0 to T_a and RH, respectively, as determined using
 383 multiple linear regressions for each urban cluster (Fig. 3a). Since T_a and RH have widely
 384 different range of values, we also consider a standardized form of this representation, given by:

$$385 \quad HI_0 = \alpha_{1, \text{std}} \frac{T_a}{T_{a,r}} + \alpha_{2, \text{std}} \frac{RH}{RH_r} \quad (18)$$

386 where $T_{a,r}$ and RH_r are the corresponding mean values for the rural backgrounds and the
 387 standardized sensitivities are $\alpha_{1, \text{std}}$ and $\alpha_{2, \text{std}}$ (Fig. 3b). A similar linear model is also used to
 388 express ΔHI_0 as a function of ΔT_a and ΔRH .



389

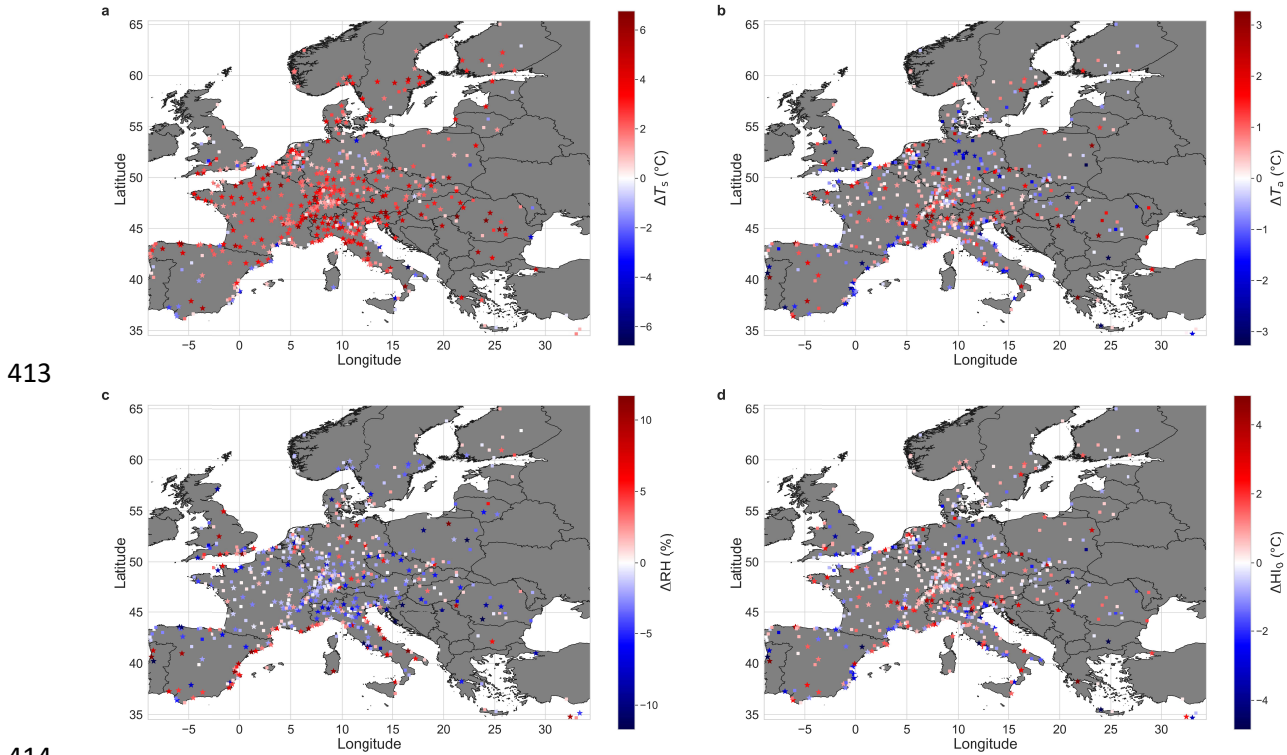
390 **Fig. 3** Control of air temperature and relative humidity on heat stress. Values of coefficients of
 391 multi-linear regressions (of the form $HI_0 = \alpha_1 T_a + \alpha_2 RH$) for all urban clusters in Europe that
 392 have sufficient data for **a** Aqua and **b** Terra overpass times, respectively. The _{std} values
 393 correspond to similar multi-linear regressions, but with standardized variables (i.e. $HI_0 = \alpha_{1,std} \frac{T_a}{T_{a,r}}$
 394 $+ \alpha_{2,std} \frac{RH}{RH_r}$) where _r variables are for the rural background.

395 3. Results

396 3.1 Urban-rural differences in temperature, humidity, and heat stress

397 Across 557 urban clusters in Europe (Fig. 1a), the mean ΔT_s (urban minus rural T_s)
 398 corresponding to the Aqua satellite's daytime overpass ($\approx 1:30$ pm local time) was 2.06 °C (5th
 399 percentile = -1.3 °C; 95th percentile = 5.25 °C) based on satellite observations over 40560 unique
 400 CWSs with data availability after quality screening (Fig. 4a). At $\approx 10:30$ am local time,
 401 corresponding to the Terra satellite's daytime overpass, the mean ΔT_s over 603 clusters was
 402 slightly lower at 1.68 °C (5th percentile = -1.22 °C; 95th percentile = 4.48 °C; Fig. S2a). In
 403 contrast, the mean urban-rural difference in T_a (ΔT_a) from the CWS measurements was only 0.12
 404 °C (5th percentile = -1.92 °C; 95th percentile = 2.19 °C) at $\approx 1:30$ pm (Fig. 4b) and 0.05 °C (5th
 405 percentile = -2.18 °C; 95th percentile = 2.17 °C) at $\approx 10:30$ am (Fig. S2b). The lower ΔT_a than
 406 ΔT_s during daytime is consistent with previous results from various data sources and at multiple
 407 scales (Chakraborty et al., 2017; Du et al., 2021; Ho et al., 2016; Hoffman et al., 2020; Venter et
 408 al., 2021; Zhang et al., 2014). Urban areas are also generally drier than their surroundings, with a
 409 mean urban-rural difference in RH (ΔRH) of -0.6% (5th percentile = -7.16% ; 95th percentile =
 410 6.43%) for the Aqua daytime overpass (Fig. 4c). The mean HI_0 at urban CWSs is slightly higher

411 than that for rural CWSs (mean urban-rural difference in HI_0 (ΔHI_0) = 0.08 °C; 5th percentile = -
 412 2.28 °C; 95th percentile = 2.58 °C; Fig. 4d).



414 **Fig. 4** Urban-rural differences for Aqua day across urban clusters. Spatial distribution of urban-
 415 rural differences in **a** radiative skin temperature (ΔT_s), **b** air temperature (ΔT_a), **c** relative
 416 humidity (ΔRH), and **d** heat index (ΔHI_0) for urban clusters in Europe at $\approx 1:30$ pm local time.
 417 The stars represent clusters with statistically significant ($p < 0.01$) differences between urban and
 418 rural values.
 419

420 Evidently, due to differences in urban and rural characteristics as well as uncertainties and lack
 421 of statistical representativeness of the measurements, there are large variabilities. However, the
 422 larger scale patterns are consistent, with 87.6% (488) of the clusters showing positive ΔT_s (with
 423 73.1% showing statistically significant differences from zero at the significance level of 0.01),
 424 which goes down to 55.1% for positive ΔT_a (37% with statistically significant differences) and
 425 54.8% for positive ΔHI_0 (31.8% with statistically significant differences) for the Aqua daytime
 426 overpass. Similar patterns are seen corresponding to the Terra daytime overpass (Fig. S2). In
 427 both cases, urban areas are generally drier than their surroundings or ΔRH is negative (59.8% of
 428 clusters at $\approx 1:30$ pm and 58.8% at $\approx 10:30$ am), which would reduce HI_0 , all else remaining

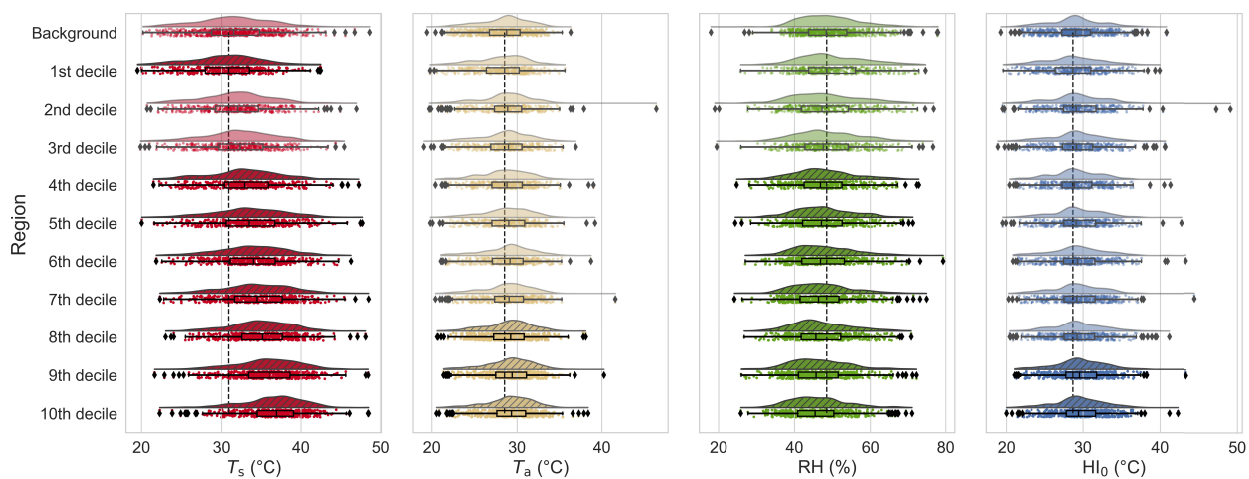
429 constant. We find ΔT_a to be over eleven times more important for modulating ΔHI_0 than ΔRH
430 (correlation coefficients of 1.37 and 0.12 for ΔT_a and ΔRH , respectively, from a multiple linear
431 regression). Although the compensating effects of T_a and RH on HI_0 makes conceptual sense,
432 what is surprising is that the urban-rural differences in HI_0 is so close to zero for cities during a
433 heatwave period, with less than a third showing statistically significant differences between the
434 urban area and its rural reference. These results weaken a common premise in many previous
435 studies where increased urban T_s is expected to indicate adverse urban impact on overall heat
436 vulnerability (Hsu et al., 2021; Manoli et al., 2019; Mentaschi et al., 2022; L. Zhao et al., 2017).

437 Consistent with previous observational and modeling estimates (Chakraborty & Lee, 2019;
438 Manoli et al., 2019; L. Zhao et al., 2014), ΔT_s is higher for wetter climate and lower for drier
439 areas, as seen when binned by quartiles of precipitation rate or accumulated precipitation for the
440 same period (Figs. S3a, S3e). However, this relationship with background climate weakens for
441 ΔT_a (Figs. S3b, S3f) and almost disappears for ΔHI_0 (Figs. S3d, S3h), evidently due to
442 thermodynamic moisture feedback through ΔRH (Figs. S3c, S3g). As such, generalized
443 mitigation strategies derived from information about background climate (Manoli et al., 2019)
444 may reduce ΔT_s but would have a much smaller impact on ΔHI_0 .

445 **3.2 Spatial gradients in the urban thermal environment**

446 Several studies (Benz & Burney, 2021; Chakraborty et al., 2019; Hsu et al., 2021; Hulley et al.,
447 2019; Maimaitiyiming et al., 2014) have examined intra-urban variability in temperature using
448 satellite-derived T_s . To test whether T_s is a useful proxy for urban heat stress variability within
449 cities, we calculate the intra-urban gradients in T_s , T_a , RH , and HI_0 using those clusters (153 for
450 Aqua and 155 for Terra) with enough (>10) CWSs in each decile neighborhood and the rural
451 background (see Methods; Fig. 5). During the Aqua daytime overpass, the gradient of T_a along
452 the decile neighborhoods is weaker than that for T_s , with 121 of the 153 clusters showing a
453 positive slope, which goes down to 114 for HI_0 . Higher T_s decile neighborhoods are generally
454 drier, with RH showing a negative slope with increasing T_s in 83.6% (128) of the clusters (Fig.
455 6a). Overall, the relationship between T_s and T_a , although positive (mean correlation coefficient r
456 = 0.34), shows a sensitivity (given by the slope of the linear regressions) much lower than 1
457 (mean slope = 0.12; Fig. 6a). This sensitivity decreases further for HI_0 (0.09) due to the

458 compensating effects of decreasing RH and increasing T_a on HI_0 (Fig. 6b). The standardized T_a
 459 rises at roughly half the rate of the decrease in standardized RH within cities, with the linear
 460 sensitivity of HI_0 to T_a being around 7 times the sensitivity to RH (Fig. 3). Consequently, the
 461 urban HI_0 in only two of the decile neighborhoods show statistically significant differences
 462 ($p < 0.01$) from the HI_0 in the rural background (Table S1). In contrast, 9, 7, and 3 of these 10
 463 neighborhoods show statistically significant differences from the background climate for T_s , RH,
 464 and T_a , respectively. Similar results are seen for other heat indices (Tables S1, S2) and
 465 corresponding to the Terra daytime overpass (Fig. S4), with 9, 2, 7, and 0 of these 10
 466 neighborhoods showing statistically significant differences from the background climate for T_s ,
 467 T_a , RH, and HI_0 , respectively.

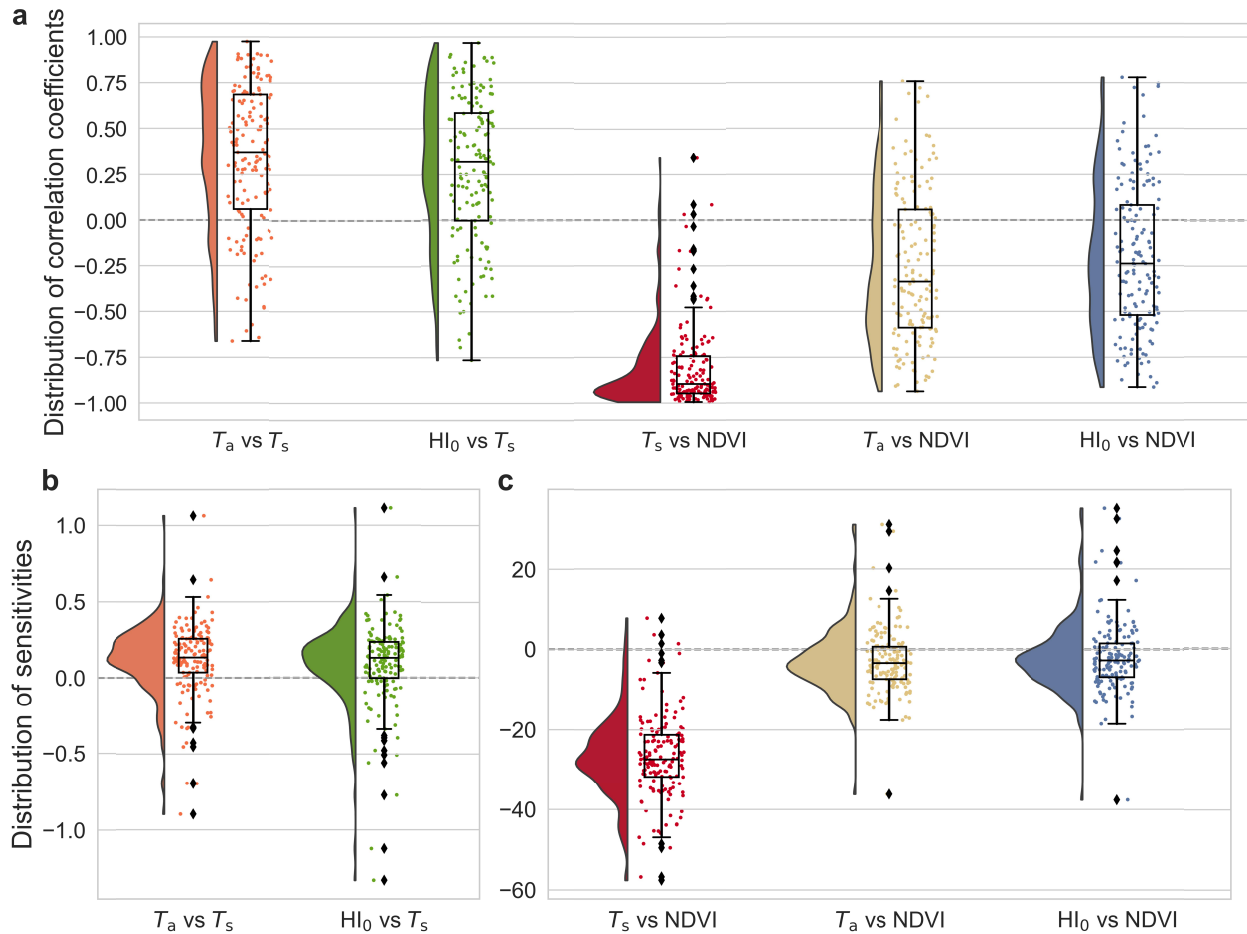


468
 469 **Fig. 5** Intra-urban gradients of variables. Distributions of composite mean surface temperature
 470 (T_s), air temperature (T_a), relative humidity (RH), and heat index (HI_0) in each of the T_s decile
 471 neighborhoods across the urban clusters considered. The vertical dashed lines mark the median
 472 of the distribution of the corresponding variable in the 1st T_s decile neighborhood. Decile
 473 neighborhoods that show statistically significant ($p < 0.01$) differences from the background
 474 reference values are shown using hatched density plots and darker shades. All calculations are
 475 for $\approx 1:30$ pm local time.

476 3.3 Role of urban vegetation

477 There is strong evidence of the cooling role urban vegetation has on T_s (Chakraborty et al., 2020;
 478 Chakraborty & Lee, 2019; Paschalis et al., 2021; Schwaab et al., 2021; Ziter et al., 2019), which
 479 is captured in our analysis. In 150 of the 153 clusters, the normalized difference vegetation index

480 (NDVI), a satellite-derived proxy for vegetation cover and vigor, is inversely correlated with T_s
481 (Fig. 6c). However, NDVI has weaker associations with T_a (mean $r = -0.81$ for T_s ; -0.26 for T_a),
482 with T_a also showing a lower sensitivity to NDVI (mean slope = -3.01 °C per unit NDVI) than T_s
483 (-26.76 °C per unit NDVI). That vegetation has a weaker control on local-scale T_a than T_s is
484 consistent with field-level observations (Novick & Katul, 2020). The association with NDVI
485 weakens further for HI_0 , with roughly 30.7% of clusters showing a positive correlation with a
486 weak mean sensitivity of around -2.15 °C per unit NDVI. Similar results are seen at $\approx 10:30$ am,
487 with 97.4% (151), 67.7% (105), and 63.2% (98) of the clusters showing a negative association
488 with NDVI in the decile neighborhoods for T_s , T_a , and HI_0 , respectively (Fig. S5c). The mean
489 sensitivities to NDVI at $\approx 10:30$ am range between -22.71 °C for T_s to -2.81 °C for HI_0 . Similarly,
490 the intra-urban variability in ΔHI_0 is weakly associated with $\Delta NDVI$ for both the Aqua and Terra
491 daytime overpasses (coefficient of determination $r^2 \leq 0.02$; Figs. 7h, S6h) compared to ΔT_s ($r^2 \approx$
492 0.30 ; Figs. 7e, S6e). The associations between ΔHI_0 and $\Delta NDVI$ are similarly weak at night (Fig.
493 S7).



494

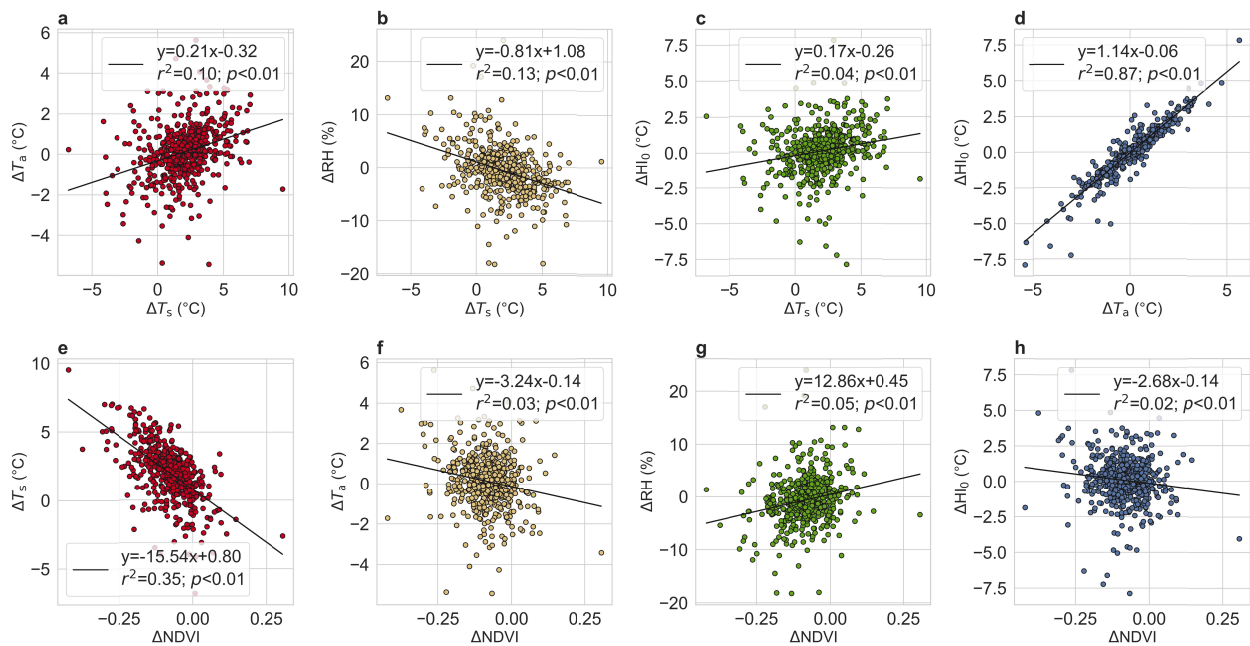
495

496 **Fig. 6** Associations between variables within urban clusters. Sub-fig **a** shows the distributions of
 497 the correlation coefficient (r) of linear regressions between surface temperature (T_s) and air
 498 temperature (T_a), T_s and heat index (HI_0), Normalized Difference Vegetation Index (NDVI) and
 499 T_s , NDVI and T_a , and NDVI and HI_0 , respectively, for urban clusters in Europe. Each data point
 500 is from a linear regression between pairs of variables for a cluster. The linear regressions have a
 501 sample size of ten (one for each T_s decile neighborhood). Sub-fig **b** and **c** show the distributions
 502 of the slope of those linear regressions, or the sensitivity of one variable to unit changes in the
 503 other. The unit of sensitivity in Sub-fig **c** is $^{\circ}\text{C}$ per unit NDVI. All calculations are for $\approx 1:30$ pm
 504 local time.

505 **4. Discussion**

506 **4.1 Deficiencies in radiative skin temperature for studying urban areas**

507 Satellite-derived T_s is widely used for urban research (Benz & Burney, 2021; Chakraborty &
 508 Lee, 2019; Clinton & Gong, 2013; Li et al., 2019; Manoli et al., 2019; Paschalis et al., 2021; L.
 509 Zhao et al., 2014). For observational studies, this is due to the availability of global and spatially
 510 continuous satellite measurements, which enable, among other things, analyses of intra-urban
 511 and inter-urban variability; difficult using ground-based measurements. Satellite-derived T_s is
 512 also used to develop and evaluate models (Li et al., 2019; Manoli et al., 2019; L. Zhao et al.,
 513 2014). Conceptual models of T_s are easier to formulate than those for T_a or HI_0 , due to strong
 514 coupling between T_s and the surface energy budget. Although T_s and T_a are not strongly
 515 correlated over urban areas, especially relevant for public health (Ho et al., 2016; Stone Jr et al.,
 516 2019), studies have assumed, either implicitly or explicitly, that ΔT_s can still be useful for
 517 making decisions about urban heat mitigation (Benz & Burney, 2021; Chakraborty et al., 2020;
 518 Hsu et al., 2021; Hulley et al., 2019; Manoli et al., 2019; L. Zhao et al., 2014). We find that for
 519 cities in Europe during a heatwave period, the correlations between urban-scale ΔT_s and ΔT_a are
 520 fairly weak, particularly during daytime ($r^2 = 0.10$ for Aqua; 0.09 for Terra; Figs. 4a, S6a), with
 521 only 21% of the variability in ΔT_s (slope = 0.21) among cities expected for ΔT_a .



522

523 **Fig. 7** Associations between variables across urban clusters. Associations between urban-rural
524 differences in **a** radiative skin temperature (ΔT_s) and air temperature (ΔT_a), **b** ΔT_s and relative
525 humidity (ΔRH), **c** ΔT_s and heat index (ΔHI_0), **d** ΔT_a and ΔHI_0 , **e** Normalized Difference
526 Vegetation Index ($\Delta NDVI$) and ΔT_s , **f** $\Delta NDVI$ and ΔT_a , **g** $\Delta NDVI$ and ΔRH , and **h** $\Delta NDVI$ and
527 ΔHI_0 across urban clusters in Europe. Each dot represents one cluster, and the lines and
528 equations of best fit are shown. All calculations are for $\approx 1:30$ pm local time.

529 Furthermore, our analysis shows that the inter-urban variability in ΔHI_0 is weaker still when
530 correlated with that of satellite-derived ΔT_s ($r^2 = 0.04$; Figs. 7c, S6c), making T_s a poor proxy for
531 the urban impact on heat vulnerability. As such, any insights gained using T_s , whether using
532 observations or models, may not be strongly relevant for mitigating urbanization-induced heat
533 stress. Note that we examine urban-rural differences to isolate the urban influence on these
534 variables, rather than absolute heat stress, which would regulate total heat-related hazard in cities
535 (Martilli et al., 2020). This is done to account for differences in absolute heat stress in cities due
536 to background climate.

537 Coarse to medium-resolution T_s from satellites have been used for hotspot analysis within cities
538 (Hulley et al., 2019; Maimaitiyiming et al., 2014). Several studies have taken advantage of the
539 spatial continuity of satellite observations to map intra-urban variability of T_s across cities, with
540 implications for environmental disparities (Benz & Burney, 2021; Chakraborty et al., 2019; Hsu
541 et al., 2021). We find that for the cities considered here, T_s is a poor proxy for the intra-urban
542 variability in HI_0 or other heat indices (including Humidex, used in heat warning systems). Even
543 the 95th and 98th percentiles of hourly HI_0 ($HI_{0,95}$ and $HI_{0,98}$, respectively) do not show
544 statistically significant differences from the background in most of the decile neighborhoods
545 (Fig. S8 and Table S3). Future multi-city studies should focus on covariance of heat stress with
546 socioeconomic variables to re-evaluate the magnitude of these environmental disparities, if any.

547 This is not to say that examining T_s over cities is pointless. Nighttime ΔHI_0 ($\approx 1:30$ am local
548 time) is generally positive (Fig. S9), and moderately correlated with ΔT_s ($r^2 = 0.21$; $p < 0.01$)
549 across (Fig. S7c) and within cities (Table S4), which might explain why previous studies have
550 shown associations between nighttime T_s and heat-related mortality (Laaidi et al., 2012; Murage
551 et al., 2017). Moreover, high T_s does increase radiant heat exposure and is the lower boundary
552 for the atmospheric column, which consequently modulates the surface energy budget and local

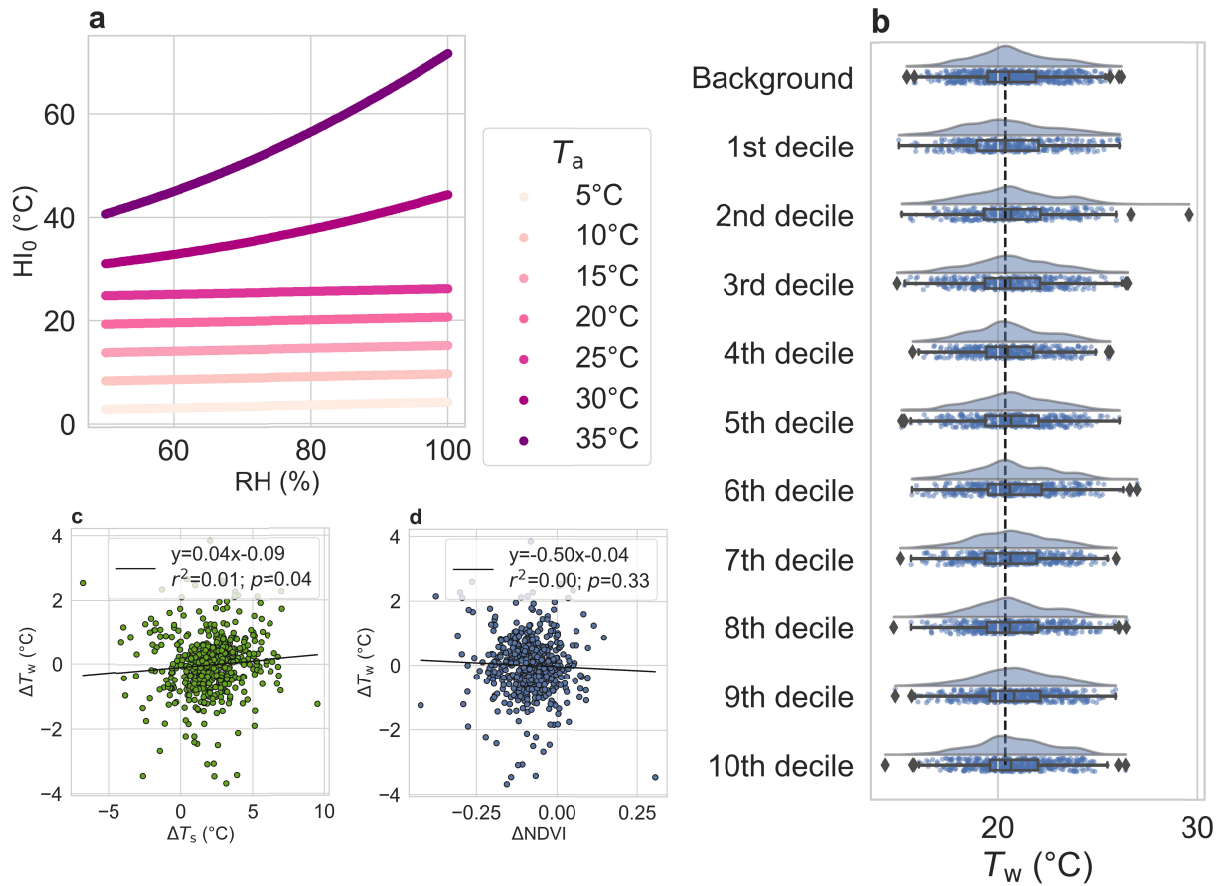
553 weather (Arnfield, 2003). Ultimately, more accurate estimates of heat stress within cities requires
554 more ground-level observations, not just of standard meteorological variables, but also exposure
555 to radiation and wind speed, which are not available from these CWSs. Moreover, CWS sensors
556 are not research-grade and frequently influenced by less-than-ideal placement, insufficient site
557 metadata, and usually lack radiation shields (Venter et al., 2021), though that last issue has
558 minimal impact since we primarily deal with distributions, not absolute values (Fig. 2).

559 Urban climate research has generally encouraged urban tree planting due to their local
560 evaporative cooling potential (Chakraborty & Lee, 2019; Li et al., 2019; Paschalis et al., 2021;
561 Schwaab et al., 2021; Wong et al., 2021; Ziter et al., 2019). However, reductions in T_s through
562 evaporation, which is the primary focus of these studies, do not imply equivalent reductions in T_a
563 (Novick & Katul, 2020). This is further complicated when we consider HI_0 due to the local-scale
564 increase in RH due to vegetation (Krayenhoff et al., 2021; Meili et al., 2020). We find that the
565 efficiency of reducing HI_0 within cities using urban vegetation is weakened (-2.15 °C for a
566 hypothetical unit change in NDVI, spanning half the physically possible range), as seen from the
567 linear correlations, due to the competing effects of reduced T_a and enhanced RH. Moreover, the
568 urban-rural differences in vegetation are not associated with the urban-rural differences in HI_0
569 across cities due to these same competing effects (Figs. 7f, 7g, S6f, S6g). However, note that
570 shading effect of trees is also important and reduces the radiant heat exposure on pedestrians at
571 the micro scale, although urban form can also serve this purpose (Middel et al., 2021; Q. Zhao et
572 al., 2018). Moreover, there are several co-benefits of urban vegetation, from increased carbon
573 sequestration to reduced air pollution to multiple beneficial health outcomes, beyond any
574 reduction in local T_s (Fargione et al., 2018; Fong et al., 2018; Remme et al., 2021). Overall,
575 mitigation strategies that rely on urban vegetation should carefully consider the realistic
576 efficiency of street trees to improve thermal comfort at multiple scales (versus competing
577 strategies) in addition to those other factors for cost-benefit analyses. As an aside, when the
578 reduction in satellite-derived T_s due to surface vegetation is usually examined (Paschalis et al.,
579 2021; Schwaab et al., 2021; Wong et al., 2021), what is compared is the association of T_s of the
580 top of the canopy (what the satellite sees) with some measure of vegetation. Since this is not
581 physically equivalent to what a pedestrian would feel either underneath the tree canopy or near it,
582 we need to be cautious about quantitative estimates of the cooling potential of urban vegetation
583 derived from satellite measurements of T_s . Similarly, models used to examine urban heat stress

584 or urban heat mitigation must incorporate accurate urban vegetation to represent realistic cities,
585 which is currently missing, simplistic, or still under development (Krayenhoff et al., 2020, 2021;
586 Meili et al., 2020; L. Zhao et al., 2017, 2021).

587 **4.2 Relative importance of humidity for heat stress**

588 The role of humidity in human physiological response to heat is well-recognized in the
589 epidemiological literature (Anderson et al., 2013). How important humidity is relative to T_a for
590 heat stress is however still an open question (Anderson et al., 2013; Sherwood, 2018). For
591 Europe, we find T_a to be around seven times more important than RH for capturing both the
592 inter-urban and intra-urban variability in HI_0 (Fig. 3). However, HI_0 is known to have a low
593 sensitivity to RH than many other heat indices (Sherwood, 2018). Moreover, most parts of
594 Europe, even at their warmest, would have a further lower sensitivity of heat stress to RH due to
595 the HI_0 formulation (Eqs 1, 2; Fig. 8a). This is particularly apparent at night, when T_a and HI_0 are
596 found to be strongly coupled (Fig. S7d) since it uses the simple linear equation (Eq. 1) with
597 much higher importance given to T_a . Since the impact of RH on HI_0 increases non-linearly with
598 increasing T_a (Fig. 8a), in warmer and more humid regions, such as in the tropics, decreasing RH
599 due to urbanization could have more noticeable effect on moderating urbanization-induced heat
600 stress (Mishra et al., 2020). As an aside, the similar magnitudes of changes in T_a and HI_0 , say
601 when correlated with NDVI (Figs. 6c, 7f, 7h), can be misleading without contextualizing that
602 unit changes in HI_0 are not physiologically equivalent to a unit change T_a . For instance, changing
603 T_a from 5 to 35 °C leads to changes in HI_0 from 5 °C to over 70 °C (Fig. 8a). Ideally, these
604 variables should be compared in the context of public health, though heat-related health-outcome
605 data are generally not available at such scales.



608 **Fig. 8** Humidity and metrics of heat stress. Sub-figure **a** shows the dependence of the heat index
 609 (HI_0) used by the US National Weather Service on relative humidity (RH) for different values of
 610 air temperature (T_a). Sub-figure **b** shows distributions of composite mean surface wet-bulb
 611 temperature (T_w) in each of the T_s decile neighborhoods across the urban clusters considered
 612 (similar to Fig. 5). Sub-figure **c** and **d** show associations between urban-rural differences in
 613 radiative skin temperature (ΔT_s) and T_w (ΔT_w), and Normalized Difference Vegetation Index
 614 ($\Delta NDVI$) and ΔT_w , respectively across urban clusters in Europe. Each dot represents one cluster
 615 and the lines and equations of best fit are shown. All calculations in sub-figures **b**, **c**, and **d** are
 616 for $\approx 1:30$ pm local time.

617 Several recent climate-related studies have also used T_w as a heat stress metric (Mishra et al.,
 618 2020; Raymond et al., 2020; L. Zhao et al., 2021). In contrast to the empirical measures of heat
 619 stress, T_w has a clear thermodynamic basis, with values above 35 $^{\circ}C$ inducing hyperthermia in
 620 humans and other mammals, and even lower values of T_w having mortality and morbidity

621 impacts (Raymond et al., 2020; Sherwood & Huber, 2010). T_w is more strongly controlled by
622 humidity than HI_0 , since it is essentially a measure of the moisture content of an air parcel. This
623 higher sensitivity of T_w to RH can be illustrated by calculating urban-rural differences in T_w
624 (ΔT_w). ΔT_w is slightly negative (-0.002 °C) and shows even weaker (and statistically
625 insignificant) correlations with ΔT_s and $\Delta NDVI$ (Figs. 8c, 8d). Moreover, none of the decile
626 regions show statistically significant differences in T_w from the background (Fig 8b). As such,
627 although the moderating effect of decreasing RH on heat stress is both conceptually and
628 observationally apparent, in the absence of health outcome data, the magnitude of this effect
629 would depend on the measure of heat stress used. For use of T_w as a heat index, it should be kept
630 in mind that only higher absolute values (above 31 °C) are valid for describing human
631 physiological response under specific conditions (completely wet and unclothed; Sherwood,
632 2018).

633 **4.3 Implications**

634 The results of the present study do not necessarily imply that urban areas have no additional heat
635 stress compared to their surroundings or that we should not target cities for heat mitigation.
636 Urban areas tend to have positive nighttime ΔT_a and ΔHI_0 , which contributes to mortality and
637 morbidity during heatwaves (Laaidi et al., 2012; Murage et al., 2017). Even during daytime, we
638 find large variabilities in ΔHI_0 , and the positive ΔHI_0 would disproportionately impact public
639 health given the high population densities in cities. Moreover, a source of uncertainty with CWS
640 data is that they have sampling biases, with most sensors set up in residential areas, not in
641 commercial districts where it is usually hotter (Hulley et al., 2019). Thus, we may be
642 systematically avoiding non-residential areas when using CWS data, where pedestrians may still
643 be exposed to higher-than-expected heat stress.

644 The caveats above do not undermine the observation that within cities, urbanization-induced
645 lower RH partly compensates for the higher T_a when it comes to heat stress, and the spatial
646 variability in this heat stress is poorly captured by satellite observations for the corresponding
647 overlaying pixels. Although cities in other parts of the world may show differences in the
648 strength, or lack thereof, of associations between these variables, on a conceptual level, we
649 speculate that we will get qualitatively similar results, with T_s showing stronger variability than
650 T_a and heat stress across scales. However, more observations are necessary to confirm this

651 hypothesis. In summary, we find compelling observational evidence that relying on T_s to
652 generate large-scale insights on the magnitude of urban heat stress and recommendations for
653 urban heat mitigation may be inappropriate. On a positive note, this mediating effect of the
654 urbanization-induced heating and drying suggest that less effort may be needed to reduce urban
655 thermal discomfort compared to their surroundings, leading to relatively higher benefits of
656 urban-scale mitigation strategies that focus on heat stress. It is often said that “You can't manage
657 what you can't measure.” Our present study suggests that we may be measuring the wrong
658 variable for quantifying and mitigating the heat-related public health consequences of
659 urbanization. In spite of the logistic and methodological simplicity of satellite-derived T_s , we
660 need more *in situ* observations of T_a , RH, wind speed, radiant heat, etc. to more accurately
661 characterize the urban thermal environment and quantify the efficiency of heat stress mitigation
662 strategies as we prepare for a warmer, wetter, and more urban future (Chen et al., 2020; W.
663 Wang et al., 2021).

664 **Acknowledgments**

665 PNNL is operated for the Department of Energy by Battelle Memorial Institute under contract
666 DE-AC05-76RL01830. The authors also thank the Yale Center for Earth Observation for
667 providing computational resources.

668 T.C. designed the study, processed the satellite scenes, analyzed the data, and wrote the first draft
669 of the manuscript. Z.S.V. extracted and processed the citizen weather station data and generated
670 the urban-rural regions of interest. Z.S.V., X.L., and Y.Q. provided inputs on methodology and
671 writing.

672 **Open Research**

673 All data will be made available through a publicly accessible repository (GitHub) on acceptance
674 of the manuscript.

675 **References**

- 676 Anderson, G. B., Bell, M. L., & Peng, R. D. (2013). Methods to Calculate the Heat Index as an Exposure Metric in
677 Environmental Health Research. *Environmental Health Perspectives*, *121*(10), 1111–1119.
678 <https://doi.org/10.1289/ehp.1206273>
- 679 Arnfield, A. J. (2003). Two decades of urban climate research: A review of turbulence, exchanges of energy and
680 water, and the urban heat island. *International Journal of Climatology*, *23*(1), 1–26.
- 681 Benz, S. A., & Burney, J. A. (2021). Widespread Race and Class Disparities in Surface Urban Heat Extremes
682 Across the United States. *Earth's Future*, *9*(7). <https://doi.org/10.1029/2021EF002016>
- 683 Bonafoni, S., Anniballe, R., & Pichierri, M. (2015). Comparison between surface and canopy layer urban heat island
684 using MODIS data. *2015 Joint Urban Remote Sensing Event (JURSE)*, 1–4.
- 685 Chakraborty, T., Hsu, A., Manya, D., & Sheriff, G. (2019). Disproportionately higher exposure to urban heat in
686 lower-income neighborhoods: A multi-city perspective. *Environmental Research Letters*, *14*(10), 105003.
687 <https://doi.org/10.1088/1748-9326/ab3b99>
- 688 Chakraborty, T., Hsu, A., Manya, D., & Sheriff, G. (2020). A spatially explicit surface urban heat island database
689 for the United States: Characterization, uncertainties, and possible applications. *ISPRS Journal of*
690 *Photogrammetry and Remote Sensing*, *168*, 74–88. <https://doi.org/10.1016/j.isprsjprs.2020.07.021>
- 691 Chakraborty, T., & Lee, X. (2019). A simplified urban-extent algorithm to characterize surface urban heat islands on
692 a global scale and examine vegetation control on their spatiotemporal variability. *International Journal of*
693 *Applied Earth Observation and Geoinformation*, *74*, 269–280. <https://doi.org/10.1016/j.jag.2018.09.015>
- 694 Chakraborty, T., Sarangi, C., & Tripathi, S. N. (2017). Understanding Diurnality and Inter-Seasonality of a Sub-
695 tropical Urban Heat Island. *Boundary-Layer Meteorology*, *163*(2), 287–309.
696 <https://doi.org/10.1007/s10546-016-0223-0>
- 697 Chen, G., Li, X., Liu, X., Chen, Y., Liang, X., Leng, J., Xu, X., Liao, W., Qiu, Y., Wu, Q., & Huang, K. (2020).
698 Global projections of future urban land expansion under shared socioeconomic pathways. *Nature*
699 *Communications*, *11*(1), 537. <https://doi.org/10.1038/s41467-020-14386-x>
- 700 Clinton, N., & Gong, P. (2013). MODIS detected surface urban heat islands and sinks: Global locations and
701 controls. *Remote Sensing of Environment*, *134*, 294–304. <https://doi.org/10.1016/j.rse.2013.03.008>

702 Da Cunha, A. R. (2015). Evaluation of measurement errors of temperature and relative humidity from HOBO data
703 logger under different conditions of exposure to solar radiation. *Environmental Monitoring and*
704 *Assessment*, 187(5), 1–11.

705 Du, H., Zhan, W., Liu, Z., Li, J., Li, L., Lai, J., Miao, S., Huang, F., Wang, C., & Wang, C. (2021). Simultaneous
706 investigation of surface and canopy urban heat islands over global cities. *ISPRS Journal of*
707 *Photogrammetry and Remote Sensing*, 181, 67–83.

708 ECA&D. (2013). *European Climate Assessment & Dataset (ECA&D)'Algorithm Theoretical Basis Document*
709 *(ATBD), Version 10.7*. Royal Netherlands Meteorological Institute KNMI.

710 Fargione, J. E., Bassett, S., Boucher, T., Bridgham, S. D., Conant, R. T., Cook-Patton, S. C., Ellis, P. W., Falcucci,
711 A., Fourqurean, J. W., Gopalakrishna, T., & others. (2018). Natural climate solutions for the United States.
712 *Science Advances*, 4(11), eaat1869.

713 Fong, K. C., Hart, J. E., & James, P. (2018). A Review of Epidemiologic Studies on Greenness and Health: Updated
714 Literature Through 2017. *Current Environmental Health Reports*, 5(1), 77–87.
715 <https://doi.org/10.1007/s40572-018-0179-y>

716 Gorelick, N., Hancher, M., Dixon, M., Ilyushchenko, S., Thau, D., & Moore, R. (2017). Google Earth Engine:
717 Planetary-scale geospatial analysis for everyone. *Remote Sensing of Environment*, 202, 18–27.
718 <https://doi.org/10.1016/j.rse.2017.06.031>

719 Heaviside, C., Macintyre, H., & Vardoulakis, S. (2017). The Urban Heat Island: Implications for Health in a
720 Changing Environment. *Current Environmental Health Reports*, 4(3), 296–305.
721 <https://doi.org/10.1007/s40572-017-0150-3>

722 Heilig, G. K. (2014). World urbanization prospects the 2014 revision. *United Nations, Department of Economic and*
723 *Social Affairs (DESA), Population Division, Population Estimates and Projections Section, New York*.

724 Ho, H. C., Knudby, A., Xu, Y., Hodul, M., & Aminipouri, M. (2016). A comparison of urban heat islands mapped
725 using skin temperature, air temperature, and apparent temperature (Humidex), for the greater Vancouver
726 area. *Science of The Total Environment*, 544, 929–938. <https://doi.org/10.1016/j.scitotenv.2015.12.021>

727 Hoffman, J. S., Shandas, V., & Pendleton, N. (2020). The Effects of Historical Housing Policies on Resident
728 Exposure to Intra-Urban Heat: A Study of 108 US Urban Areas. *Climate*, 8(1), 12.
729 <https://doi.org/10.3390/cli8010012>

730 Howard, L. (1833). *The climate of London: Deduced from meteorological observations made in the metropolis and*
731 *at various places around it* (Vol. 2). Harvey and Darton, J. and A. Arch, Longman, Hatchard, S. Highley
732 [and] R. Hunter.

733 Hsu, A., Sheriff, G., Chakraborty, T., & Manya, D. (2021). Disproportionate exposure to urban heat island intensity
734 across major US cities. *Nature Communications*, *12*(1), 2721. <https://doi.org/10.1038/s41467-021-22799-5>

735 Huang, K., Lee, X., Stone Jr, B., Knievel, J., Bell, M. L., & Seto, K. C. (2021). Persistent increases in nighttime heat
736 stress from urban expansion despite heat island mitigation. *Journal of Geophysical Research: Atmospheres*,
737 *126*(4), e2020JD033831.

738 Hulley, G., Shivers, S., Wetherley, E., & Cudd, R. (2019). New ECOSTRESS and MODIS Land Surface
739 Temperature Data Reveal Fine-Scale Heat Vulnerability in Cities: A Case Study for Los Angeles County,
740 California. *Remote Sensing*, *11*(18), 2136. <https://doi.org/10.3390/rs11182136>

741 Iribarne, J. V., & Godson, W. L. (1981). *Atmospheric thermodynamics* (Vol. 6). Springer Science & Business
742 Media.

743 Jin, M., & Dickinson, R. E. (2010). Land surface skin temperature climatology: Benefitting from the strengths of
744 satellite observations. *Environ Res Lett*, *5*(4), 044004.

745 Keith, L., Meerow, S., & Wagner, T. (2019). Planning for extreme heat: A review. *Journal of Extreme Events*,
746 *6*(03n04), 2050003.

747 Krayenhoff, E. S., Broadbent, A. M., Zhao, L., Georgescu, M., Middel, A., Voogt, J. A., Martilli, A., Sailor, D. J., &
748 Erell, E. (2021). Cooling hot cities: A systematic and critical review of the numerical modelling literature.
749 *Environmental Research Letters*, *16*(5), 053007. <https://doi.org/10.1088/1748-9326/abdcf1>

750 Krayenhoff, E. S., Jiang, T., Christen, A., Martilli, A., Oke, T. R., Bailey, B. N., Nazarian, N., Voogt, J. A.,
751 Giometto, M. G., & Stastny, A. (2020). A multi-layer urban canopy meteorological model with trees (BEP-
752 Tree): Street tree impacts on pedestrian-level climate. *Urban Climate*, *32*, 100590.

753 Laaidi, K., Zeghnoun, A., Dousset, B., Bretin, P., Vandentorren, S., Giraudet, E., & Beaudreau, P. (2012). The
754 Impact of Heat Islands on Mortality in Paris during the August 2003 Heat Wave. *Environmental Health*
755 *Perspectives*, *120*(2), 254–259. <https://doi.org/10.1289/ehp.1103532>

756 Li, D., Liao, W., Rigden, A. J., Liu, X., Wang, D., Malyshev, S., & Shevliakova, E. (2019). Urban heat island:
757 Aerodynamics or imperviousness? *Science Advances*, *5*(4), eaau4299.

758 Lokoshchenko, M. A. (2017). Urban Heat Island and Urban Dry Island in Moscow and Their Centennial Changes.
759 *Journal of Applied Meteorology and Climatology*, 56(10), 2729–2745. [https://doi.org/10.1175/JAMC-D-](https://doi.org/10.1175/JAMC-D-16-0383.1)
760 16-0383.1

761 Maia-Silva, D., Kumar, R., & Nateghi, R. (2020). The critical role of humidity in modeling summer electricity
762 demand across the United States. *Nature Communications*, 11(1), 1686. [https://doi.org/10.1038/s41467-](https://doi.org/10.1038/s41467-020-15393-8)
763 020-15393-8

764 Maimaitiyiming, M., Ghulam, A., Tiyyip, T., Pla, F., Latorre-Carmona, P., Halik, Ü., Sawut, M., & Caetano, M.
765 (2014). Effects of green space spatial pattern on land surface temperature: Implications for sustainable
766 urban planning and climate change adaptation. *ISPRS Journal of Photogrammetry and Remote Sensing*, 89,
767 59–66. <https://doi.org/10.1016/j.isprsjprs.2013.12.010>

768 Manoli, G., Fatichi, S., Schläpfer, M., Yu, K., Crowther, T. W., Meili, N., Burlando, P., Katul, G. G., & Bou-Zeid,
769 E. (2019). Magnitude of urban heat islands largely explained by climate and population. *Nature*, 573(7772),
770 55–60. <https://doi.org/10.1038/s41586-019-1512-9>

771 Martilli, A., Krayerhoff, E. S., & Nazarian, N. (2020). Is the Urban Heat Island intensity relevant for heat mitigation
772 studies? *Urban Climate*, 31, 100541. <https://doi.org/10.1016/j.uclim.2019.100541>

773 Masterton, J. M., & Richardson, F. A. (1979). *Humidex: A method of quantifying human discomfort due to excessive*
774 *heat and humidity*. Environment Canada, Atmospheric Environment.

775 Meier, F., Fenner, D., Grassmann, T., Otto, M., & Scherer, D. (2017). Crowdsourcing air temperature from citizen
776 weather stations for urban climate research. *Urban Climate*, 19, 170–191.
777 <https://doi.org/10.1016/j.uclim.2017.01.006>

778 Meili, N., Manoli, G., Burlando, P., Bou-Zeid, E., Chow, W. T. L., Coutts, A. M., Daly, E., Nice, K. A., Roth, M.,
779 Tapper, N. J., Velasco, E., Vivoni, E. R., & Fatichi, S. (2020). An urban ecohydrological model to quantify
780 the effect of vegetation on urban climate and hydrology (UT&C v1.0). *Geoscientific Model Development*,
781 13(1), 335–362. <https://doi.org/10.5194/gmd-13-335-2020>

782 Mentaschi, L., Duveiller, G., Zulian, G., Corbane, C., Pesaresi, M., Maes, J., Stocchino, A., & Feyen, L. (2022).
783 Global long-term mapping of surface temperature shows intensified intra-city urban heat island extremes.
784 *Global Environmental Change*, 72, 102441.

785 Middel, A., Alkhaled, S., Schneider, F. A., Hagen, B., & Coseo, P. (2021). 50 Grades of Shade. *Bulletin of the*
786 *American Meteorological Society*, 1–35. <https://doi.org/10.1175/BAMS-D-20-0193.1>

787 Mishra, V., Ambika, A. K., Asoka, A., Aadhar, S., Buzan, J., Kumar, R., & Huber, M. (2020). Moist heat stress
788 extremes in India enhanced by irrigation. *Nature Geoscience*, 13(11), 722–728.
789 <https://doi.org/10.1038/s41561-020-00650-8>

790 Muller, C. L., Chapman, L., Grimmond, C. S. B., Young, D. T., & Cai, X. (2013). Sensors and the city: A review of
791 urban meteorological networks: SENSORS AND THE CITY. *International Journal of Climatology*, 33(7),
792 1585–1600. <https://doi.org/10.1002/joc.3678>

793 Muñoz-Sabater, J., Dutra, E., Agustí-Panareda, A., Albergel, C., Arduini, G., Balsamo, G., Boussetta, S., Choulga,
794 M., Harrigan, S., Hersbach, H., Martens, B., Miralles, D. G., Piles, M., Rodríguez-Fernández, N. J., Zsoter,
795 E., Buontempo, C., & Thépaut, J.-N. (2021). *ERA5-Land: A state-of-the-art global reanalysis dataset for*
796 *land applications* [Preprint]. Data, Algorithms, and Models. <https://doi.org/10.5194/essd-2021-82>

797 Murage, P., Hajat, S., & Kovats, R. S. (2017). Effect of night-time temperatures on cause and age-specific mortality
798 in London: *Environmental Epidemiology*, 1. <https://doi.org/10.1097/EE9.000000000000005>

799 Napoly, A., Grassmann, T., Meier, F., & Fenner, D. (2018). Development and Application of a Statistically-Based
800 Quality Control for Crowdsourced Air Temperature Data. *Frontiers in Earth Science*, 6, 118.
801 <https://doi.org/10.3389/feart.2018.00118>

802 NASA Goddard Earth Sciences Data And Information Services Center. (2019). *GPM IMERG Final Precipitation L3*
803 *1 day 0.1 degree x 0.1 degree V06* [Data set]. NASA Goddard Earth Sciences Data and Information
804 Services Center. <https://doi.org/10.5067/GPM/IMERGDF/DAY/06>

805 Novick, K. A., & Katul, G. G. (2020). The Duality of Reforestation Impacts on Surface and Air Temperature.
806 *Journal of Geophysical Research: Biogeosciences*, 125.

807 Oleson, K. W., Monaghan, A., Wilhelmi, O., Barlage, M., Brunzell, N., Feddema, J., Hu, L., & Steinhoff, D. F.
808 (2015). Interactions between urbanization, heat stress, and climate change. *Climatic Change*, 129(3), 525–
809 541.

810 Paschalis, A., Chakraborty, T., Fatichi, S., Meili, N., & Manoli, G. (2021). Urban Forests as Main Regulator of the
811 Evaporative Cooling Effect in Cities. *AGU Advances*, 2(2). <https://doi.org/10.1029/2020AV000303>

812 Perkins-Kirkpatrick, S. E., & Lewis, S. C. (2020). Increasing trends in regional heatwaves. *Nature Communications*,
813 11(1), 3357. <https://doi.org/10.1038/s41467-020-16970-7>

814 Pesaresi, M., & Freire, S. (2016). GHS Settlement grid following the REGIO model 2014 in application to GHSL
815 Landsat and CIESIN GPW v4-multitemporal (1975-1990-2000-2015). *JRC Data Cat.*

816 Qian, Y., Chakraborty, T. C., Li, J., Li, D., He, C., Sarangi, C., Chen, F., Yang, X., & Leung, L. R. (2022).
817 Urbanization Impact on Regional Climate and Extreme Weather: Current Understanding, Uncertainties,
818 and Future Research Directions. *Advances in Atmospheric Sciences*. [https://doi.org/10.1007/s00376-021-](https://doi.org/10.1007/s00376-021-1371-9)
819 1371-9

820 Raymond, C., Matthews, T., & Horton, R. M. (2020). The emergence of heat and humidity too severe for human
821 tolerance. *Science Advances*, 6(19), eaaw1838. <https://doi.org/10.1126/sciadv.aaw1838>

822 Remme, R. P., Frumkin, H., Guerry, A. D., King, A. C., Mandle, L., Sarabu, C., Bratman, G. N., Giles-Corti, B.,
823 Hamel, P., Han, B., Hicks, J. L., James, P., Lawler, J. J., Lindahl, T., Liu, H., Lu, Y., Oosterbroek, B.,
824 Paudel, B., Sallis, J. F., ... Daily, G. C. (2021). An ecosystem service perspective on urban nature, physical
825 activity, and health. *Proceedings of the National Academy of Sciences*, 118(22), e2018472118.
826 <https://doi.org/10.1073/pnas.2018472118>

827 Rothfus, L. P., & Headquarters, N. S. R. (1990). The heat index equation (or, more than you ever wanted to know
828 about heat index). *Fort Worth, Texas: National Oceanic and Atmospheric Administration, National*
829 *Weather Service, Office of Meteorology, 9023.*

830 Rouse, J. W., Haas, R. H., Schell, J. A., Deering, D. W., & Harlan, J. C. (1974). Monitoring the vernal advancement
831 and retrogradation (green wave effect) of natural vegetation. *NASA/GSFC Type III Final Report, Greenbelt,*
832 *Md, 371.*

833 Sarangi, C., Qian, Y., Li, J., Leung, L. R., Chakraborty, T. C., & Liu, Y. (2021). Urbanization Amplifies Nighttime
834 Heat Stress on Warmer Days Over the US. *Geophysical Research Letters*, 48(24).
835 <https://doi.org/10.1029/2021GL095678>

836 Schwaab, J., Meier, R., Mussetti, G., Seneviratne, S., Bürgi, C., & Davin, E. L. (2021). The role of urban trees in
837 reducing land surface temperatures in European cities. *Nature Communications*, 12(1), 1–11.

838 Sharma, A., Wuebbles, D. J., & Kotamarthi, R. (2021). The Need for Urban-Resolving Climate Modeling Across
839 Scales. *AGU Advances*, 2(1). <https://doi.org/10.1029/2020AV000271>

840 Sherwood, S. C. (2018). How Important Is Humidity in Heat Stress? *Journal of Geophysical Research:*
841 *Atmospheres*, 123(21). <https://doi.org/10.1029/2018JD028969>

842 Sherwood, S. C., & Huber, M. (2010). An adaptability limit to climate change due to heat stress. *Proceedings of the*
843 *National Academy of Sciences*, 107(21), 9552–9555. <https://doi.org/10.1073/pnas.0913352107>

844 Steadman, R. G. (1979). The assessment of sultriness. Part I: A temperature-humidity index based on human
845 physiology and clothing science. *Journal of Applied Meteorology and Climatology*, 18(7), 861–873.

846 Stone Jr, B., Lanza, K., Mallen, E., Vargo, J., & Russell, A. (2019). Urban heat management in Louisville,
847 Kentucky: A framework for climate adaptation planning. *Journal of Planning Education and Research*,
848 0739456X19879214.

849 Stull, R. (2011). Wet-Bulb Temperature from Relative Humidity and Air Temperature. *Journal of Applied*
850 *Meteorology and Climatology*, 50(11), 2267–2269. <https://doi.org/10.1175/JAMC-D-11-0143.1>

851 Venter, Z. S., Chakraborty, T., & Lee, X. (2021). Crowdsourced air temperatures contrast satellite measures of the
852 urban heat island and its mechanisms. *Science Advances*, 7(22), eabb9569.
853 <https://doi.org/10.1126/sciadv.abb9569>

854 Wan, Z. (2006). MODIS land surface temperature products users' guide. *Institute for Computational Earth System*
855 *Science, University of California: Santa Barbara, CA, USA*, 805.

856 Wang, W., Chakraborty, T. C., Xiao, W., & Lee, X. (2021). Ocean surface energy balance allows a constraint on the
857 sensitivity of precipitation to global warming. *Nature Communications*, 12(1), 2115.
858 <https://doi.org/10.1038/s41467-021-22406-7>

859 Wang, Z., Song, J., Chan, P. W., & Li, Y. (2021). The urban moisture island phenomenon and its mechanisms in a
860 high-rise high-density city. *International Journal of Climatology*, 41(S1). <https://doi.org/10.1002/joc.6672>

861 Wilcoxon, F., Kotz, S., & Johnson, N. L. (1992). Breakthroughs in Statistics: Methodology and Distribution. *New*
862 *York, NY: Springer New York*, 196–2.

863 Wong, N. H., Tan, C. L., Kolokotsa, D. D., & Takebayashi, H. (2021). Greenery as a mitigation and adaptation
864 strategy to urban heat. *Nature Reviews Earth & Environment*, 2(3), 166–181.
865 <https://doi.org/10.1038/s43017-020-00129-5>

866 Zhang, P., Bounoua, L., Imhoff, M. L., Wolfe, R. E., & Thome, K. (2014). Comparison of MODIS land surface
867 temperature and air temperature over the continental USA meteorological stations. *Canadian Journal of*
868 *Remote Sensing*, 40(2), 110–122.

869 Zhao, L., Lee, X., & Schultz, N. M. (2017). A wedge strategy for mitigation of urban warming in future climate
870 scenarios. *Atmospheric Chemistry and Physics*, 17(14), 9067–9080. [https://doi.org/10.5194/acp-17-9067-](https://doi.org/10.5194/acp-17-9067-2017)
871 2017

872 Zhao, L., Lee, X., Smith, R. B., & Oleson, K. (2014). Strong contributions of local background climate to urban heat
873 islands. *Nature*, 511(7508), 216–219.

874 Zhao, L., Oleson, K., Bou-Zeid, E., Krayenhoff, E. S., Bray, A., Zhu, Q., Zheng, Z., Chen, C., & Oppenheimer, M.
875 (2021). Global multi-model projections of local urban climates. *Nature Climate Change*, 11(2), 152–157.
876 <https://doi.org/10.1038/s41558-020-00958-8>

877 Zhao, Q., Yang, J., Wang, Z.-H., & Wentz, E. A. (2018). Assessing the cooling benefits of tree shade by an outdoor
878 urban physical scale model at Tempe, AZ. *Urban Science*, 2(1), 4.

879 Zheng, Z., Zhao, L., & Oleson, K. W. (2021). Large model structural uncertainty in global projections of urban heat
880 waves. *Nature Communications*, 12(1), 1–9.

881 Ziter, C. D., Pedersen, E. J., Kucharik, C. J., & Turner, M. G. (2019). Scale-dependent interactions between tree
882 canopy cover and impervious surfaces reduce daytime urban heat during summer. *Proceedings of the*
883 *National Academy of Sciences*, 116(15), 7575–7580. <https://doi.org/10.1073/pnas.1817561116>

884